Comparing IOP-Induced Scleral Deformations in the Myopic and Myopic Glaucoma Spectrums

Thanadet Chuangsuwanich,[1,2] Tin A. Tun,[3,4] Fabian A. Braeu,[2,4] Rachel S. Chong,[4] Xiaofei Wang,[5] Ching-Lin Ho,[4] Tin Aung,[1,3,4] Michaël J. A. Girard,[2,3,6] and Quan V. Hoang[1,3,4,7]

[1]Yong Loo Lin School of Medicine, National University of Singapore, Singapore
[2]Ophthalmic Engineering & Innovation Laboratory, Singapore Eye Research Institute, Singapore National Eye Centre, Singapore
[3]Eye-ACP, Duke-NUS Medical School, Singapore, Singapore
[4]Singapore Eye Research Institute, Singapore National Eye Centre, Singapore
[5]Laboratory for Biomechanics and Mechanobiology of Ministry of Education, Beijing Advanced Innovation Center for Biomedical Engineering, School of Biological Science and Medical Engineering, School of Engineering Medicine, Beihang University, Beijing, China
[6]Institute for Molecular and Clinical Ophthalmology, Basel, Switzerland
[7]Department of Ophthalmology, Columbia University, New York, United States

Correspondence: Quan V. Hoang, Singapore Eye Research Institute (SERI), The Academia, 20 College Road, Discovery Tower Level 6, Singapore 169856, Singapore; donny.hoang@duke-nus.edu.sg. Michaël J.A. Girard, Ophthalmic Engineering & Innovation Laboratory (OEIL), Singapore Eye Research Institute (SERI), The Academia, 20 College Road, Discovery Tower Level 6, Singapore 169856, Singapore; mgirard@ophthalmic.engineering.

MJAG and QVH contributed equally and share corresponding and senior authorship.

Received: April 22, 2024
Accepted: October 7, 2024
Published: November 25, 2024

Citation: Chuangsuwanich T, Tun TA, Braeu FA, et al. Comparing IOP-Induced scleral deformations in the myopic and myopic glaucoma spectrums. *Invest Ophthalmol Vis Sci.* 2024;65(13):54. https://doi.org/10.1167/iovs.65.13.54

Purpose. To compare changes in macular curvature following acute IOP elevation across a range of myopic conditions.

Methods. We studied 328 eyes from 184 subjects, comprising 32 emmetropic controls (between +2.75 and −2.75 diopters), 50 eyes with high myopia (<−5 diopters; HM), 108 highly myopic with glaucoma (HMG) and 105 pathologic myopia (PM) eyes, and 33 PM with staphyloma (PM+S) eyes. For each eye, we imaged the macula using optical coherence tomography (OCT) under the baseline condition and under acute IOP elevation (to ∼40 mm Hg) achieved through ophthalmodynamometry. We manually aligned the scans (baseline and IOP elevation) using three vascular landmarks in the macula tissue. We then automatically segmented the sclera and the choroid tissues using a deep learning algorithm and extracted the sclera–choroid interface. We calculated the macula curvatures, determined by the radius of curvature of the sclera–choroid interface in the nasal–temporal and superior–inferior direction. Differences in macula curvatures between baseline and elevated IOP scans were calculated at corresponding locations, and the mean curvature difference was reported for each eye.

Results. IOP elevation resulted in a significantly higher macula curvature change along the nasal–temporal direction in the PM+S ($13.5 \pm 8.2 \times 10^{-5}$ μm^{-1}), PM ($9.0 \pm 7.9 \times 10^{-5}$ μm^{-1}), and HMG ($5.2 \pm 5.1 \times 10^{-5}$ μm^{-1}) eyes as compared to HM ($3.1 \pm 2.7 \times 10^{-5}$ μm^{-1}) eyes (all $P < 0.05$). Interestingly, HM and HMG eyes had the same curvature change in the nasal–temporal direction as emmetropic control eyes ($4.2 \pm 4.3 \times 10^{-5}$ μm^{-1}).

Conclusions. Our findings indicate that the macula in HMG, PM, and PM+S eyes showed greater curvature changes under IOP elevation compared to HM and emmetropic eyes. These preliminary results suggest that HM eyes with conditions such as glaucoma or staphyloma are more sensitive to acute IOP elevation.

Keywords: high myopia with glaucoma, staphyloma, biomechanics, macula deformation, sclera

It is well established that the sclera plays a pivotal role in the etiology of high myopia and pathologic myopia, as scleral remodeling stands as one of the key factors in myopia development.[1] Anomalous deformation and elongation of the scleral wall in individuals with high myopia may also give rise to myopic maculopathy, encompassing conditions such as posterior staphyloma, which substantially elevates the risk of vision impairment.[2] Furthermore, various myopia-related abnormalities, such as macular holes, myopic foveoschisis, and dome-shaped maculopathy, have been attributed to the intricate interplay of tractional forces acting on the posterior sclera within the macular region.[3] Thus, the biomechanics of the sclera, especially within the macular region, could be one of the key factors in the development of high myopia and pathologic myopia. Unfortunately, few studies have emerged on investigating the biomechanics of the sclera in the macula region.[4–6] Park et al.[5] quantified the two-dimensional deformation of the macular region before and after macula hole surgery through the analysis of fundus images and reported significant

correlations between the extent of macula deformation and the occurrences of metamorphosia. In another study, Spaide et al.[4] found that foveal deformation correlates with the diameter of the vitreous detachment. Our prior studies have delved into characterizing the optic nerve head (ONH) deformations under IOP elevation and eye movements within diverse subject cohorts,[7] including those with myopia-related disorders.[8] Notably, we found that ONH deformation under IOP elevation was distinct among those with high myopia (HM) and high myopia coexisting with glaucoma. Building upon this foundation, we postulate that the deformation of the sclera in the macular region during acute IOP elevation may emerge as a distinct biomechanical marker, showcasing variability across various myopia-related conditions.

The biomechanical properties of the sclera, encompassing factors like geometry, thickness, and collagen fiber arrangement, are known to exert significant influences on the biomechanical environment of the ONH.[9] Alterations in the posterior sclera, such as thinning, weakening, and the depletion of collagen and proteoglycans, which are associated with high myopia, may heighten the biomechanical vulnerability of the ONH, thereby increasing the risk of glaucoma.[1,10–12] Numerous clinical and population-based studies have established a connection between glaucoma and myopia.[13–15] However, diagnosing glaucoma accurately in highly myopic patients remains a challenge. Traditional glaucoma diagnostic markers, such as ONH appearance, peripapillary atrophy, and visual field defects,[16,17] often become obscured by structural changes commonly found in HM and pathologic myopia (PM). Therefore, a new biomarker capable of distinguishing between glaucoma eyes, myopic eyes, or a combination of both would be valuable in clinical practice.

In this study, we aimed to assess the biomechanics of the sclera within the macula region under elevated IOP in control patients and patients with a range of myopia-related conditions, including HM, PM, PM with staphyloma (PM+S), and those with a definitive diagnosis of both myopia and glaucoma (HMG). Our goal is to better understand how different pathologies influence the macula tissues' (retina, choroid, and sclera) sensitivity to external loads.

Methods

Subject Recruitment

We studied 328 eyes from 184 subjects, which comprised 32 emmetropic controls (between +2.75 and −2.75 diopters), 50 HM eyes, 108 HMG eyes, and 138 PM eyes, which were identified during their regularly scheduled general, retina, and/or glaucoma clinic visits at the Singapore National Eye Centre. We included subjects aged more than 50 years and of Chinese ethnicity (predominant in Singapore) and excluded subjects who underwent prior intraocular/orbital/brain surgeries; those with a history of strabismus, ocular trauma, ocular motor palsies, or orbital/brain tumors; patients with clinically abnormal saccadic or pursuit eye movements; subjects with poor lamina cribrosa (LC) visibility in OCT (<50% en face visibility)[18]; subjects with known carotid or peripheral vascular disease; or those with any other known pathologic ocular conditions.

Control eyes had a refractive error between +2.75 and −2.75 diopters with axial lengths less than 25 mm. Control eyes had normal IOP and no pathologic features on the ONH and the retina. HM was defined by eyes with axial lengths greater than 25 mm and myopic refraction <−5 diopters. HMG was defined as eyes with both HM (excluding PM and staphyloma) and a clinical glaucoma diagnosis by a glaucoma specialist (RSC, AT). PM (without staphyloma) was defined for eyes exhibiting both HM and myopic macular degeneration, as defined by the meta-analysis for the PM classification system,[19] or myopic traction maculopathy. PM+S was defined as HM eyes with a clinical diagnosis of staphyloma based on multimodal imaging (fundus photography, optical coherence tomography, ultrasonography, and, in selected subjects, magnetic resonance imaging) and confirmed by a retinal specialist (QVH).

Glaucoma was defined as glaucomatous optic neuropathy (based on Nagaoka et al.[20]), characterized as a loss of the neuroretinal rim with a vertical cup-to-disc ratio >0.7 or focal notching with a nerve fiber layer defect attributable to glaucoma (based on clinical observation) and/or asymmetry of the cup-to-disc ratio between eyes >0.2, with repeatable glaucomatous visual field defects (independent of the IOP value) in at least one eye.

Each eye underwent the following ocular examinations: (1) measurement of refraction using an autorefractor/keratometer (RK-5; Canon, Tokyo, Japan) and (2) measurement of axial length, central corneal thickness, and anterior chamber depth using a commercial device (Lenstar LS 900; Haag-Streit AG, Köniz, Switzerland). For each tested eye, we performed a visual field test using a standard achromatic perimetry with the Humphrey Field Analyzer (Carl Zeiss Meditec, Dublin, CA, USA).

This study was approved by the SingHealth Centralized Institutional Review Board and adhered to the tenets of the Declaration of Helsinki. Written informed consent was obtained from each subject.

OCT Imaging

Subjects' pupils were dilated with 1.0% tropicamide before imaging with spectral-domain OCT (Spectralis; Heidelberg Engineering GmbH, Heidelberg, Germany). The imaging protocol was similar to that from our previous work.[21] In brief, we conducted a raster scan of the macula region (covering a rectangular region of 15° × 10° centered at the fovea), comprising 97 serial B-scans, with each B-scan comprising 384 A-scans (Fig. 1A). The scan area was approximately 4.7 mm long (nasal–temporal direction) and 3.1 mm wide (superior–inferior direction). Our coordinate system was defined as x: nasal–temporal direction, y: superior–inferior direction, and z: anterior–posterior direction. The pixel resolutions along the x, y, and z directions were 11.5 ± 0.6 µm, 35.1 ± 1.0 µm, and 3.87 µm, respectively.

OCT Imaging During Acute IOP Elevation

In this study, ophthalmodynamometry was employed to acutely raise IOP and induce deformation in the tissues of the macula region. We first measured the subjects' baseline IOP using a Tono-Pen (Reichert Instruments GmbH, Munich, Germany). We then applied a constant force of 0.65 N to the temporal side of the lower eyelid using an ophthalmodynamometer, as per an established protocol.[21–24] The force was sustained for approximately 2 to

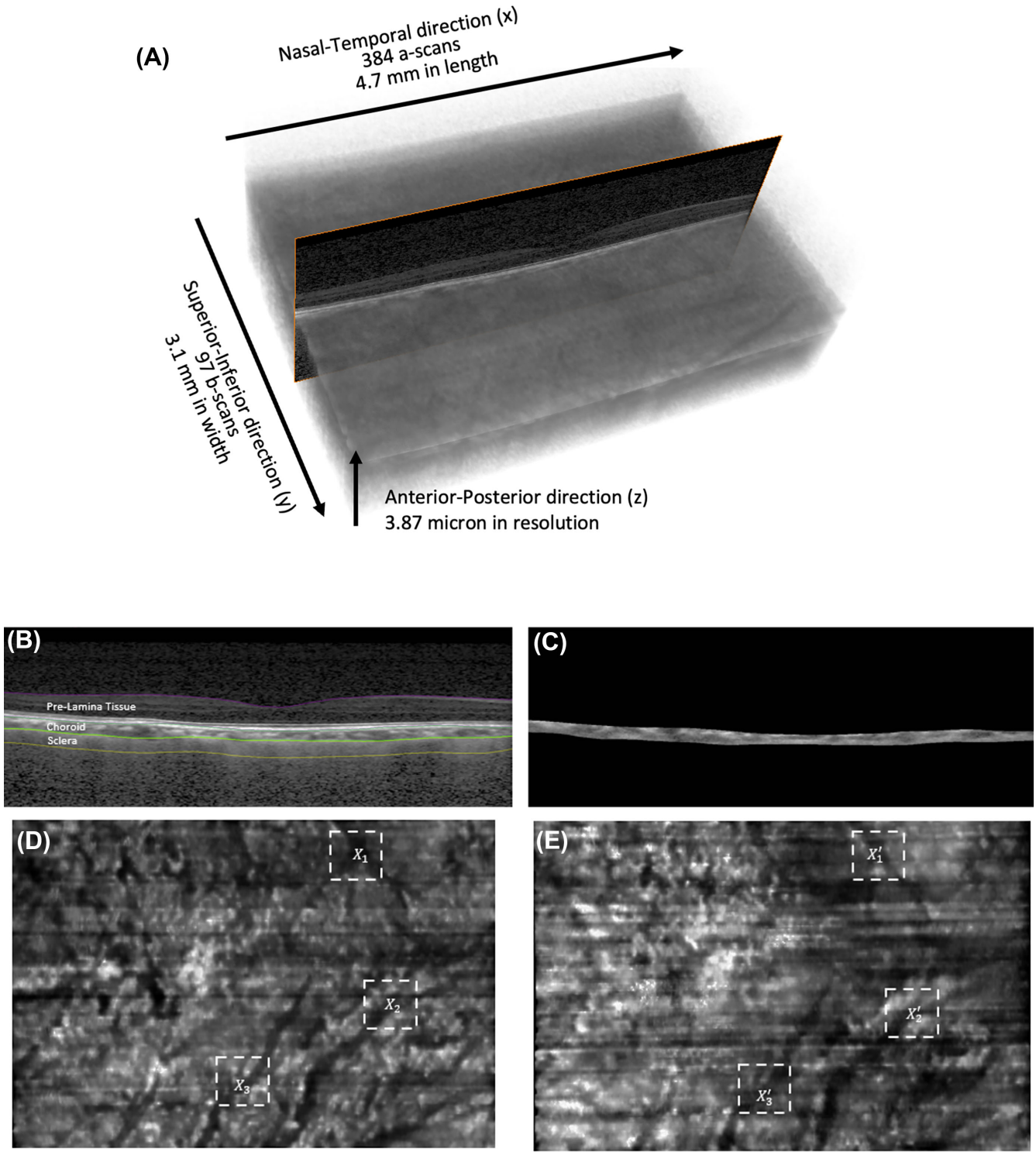

Figure 1. (**A**) OCT scans of the macula region with coordinates definition and dimension. (**B**) Segmentation of prelamina tissue, choroid, and sclera from a single B-scan. (**C**) Extraction of choroid tissue from B-scans. (**D**) Projected choroidal image of baseline volume, showing blood vessels in *black*. (**E**) Projected choroidal image of IOP-elevated volume, showing blood vessels in *black*. X_n is the bifurcation that corresponds with X'_n for each eye.

3 minutes during the entire OCT scan. The applied force elevated the IOP to approximately 35 mm Hg and was consistently maintained. IOP was then reassessed with a Tono-Pen, and the ONH was imaged with OCT in the baseline position immediately (within 30 seconds) after the IOP measurement.

Registration of Baseline Macula Scans and IOP Elevated Scans

To ensure proper spatial alignment on the x–y plane for the baseline scan and elevated IOP scan, we employed manual rigid body registration. This process involved using

Investigative Ophthalmology & Visual Science

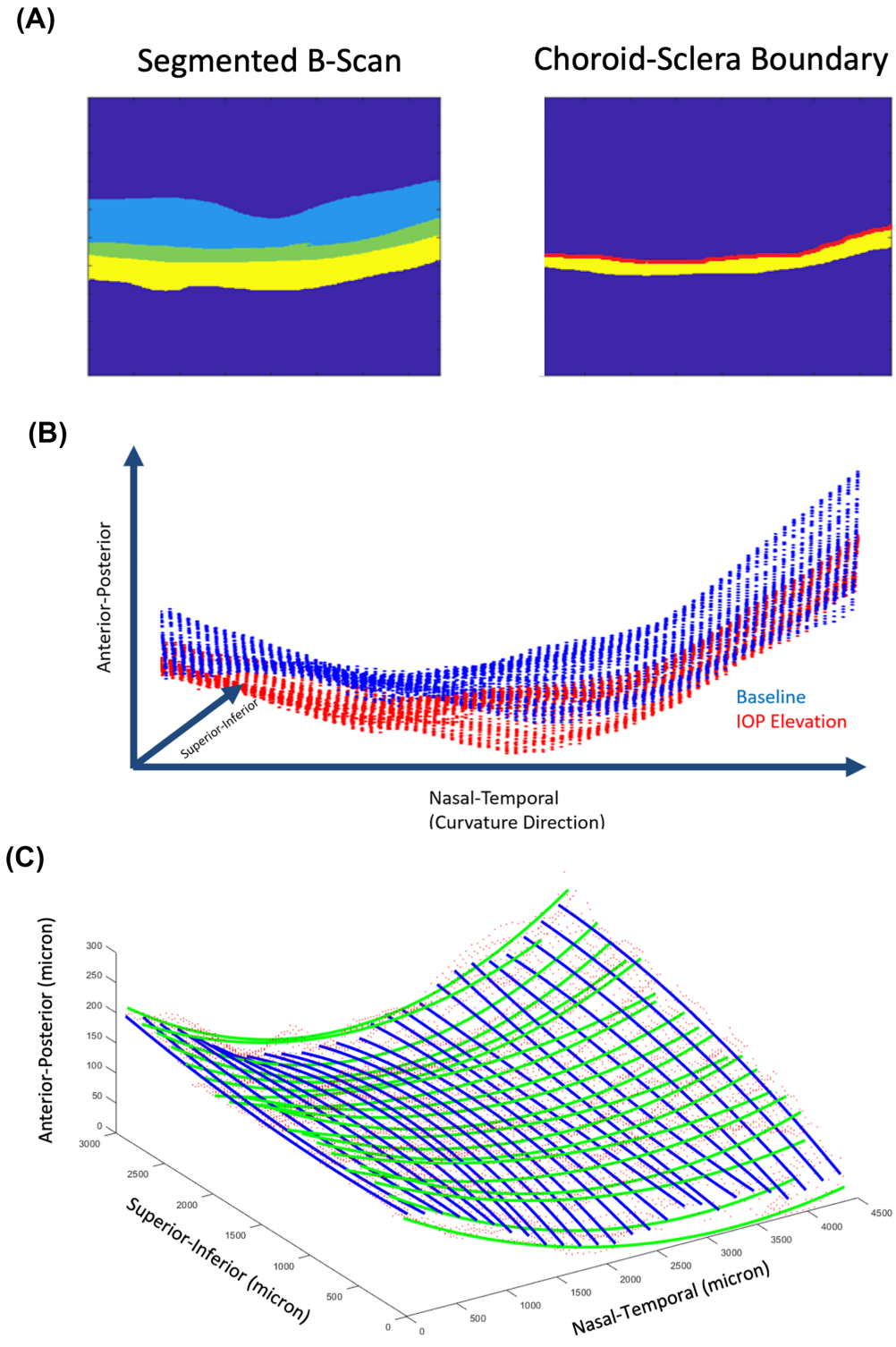

Figure 2. (**A**) Example of a segmentation from a B-scan (*light blue* region represents prelamina tissue, *green* represents choroid tissue, and *yellow* represents sclera tissue) and an example of the choroid–sclera boundary used to extract point clouds in *red*. (**B**) Point clouds from the choroid–sclera boundary of an eye. *Blue* represents the point cloud from the baseline volume, and *red* represents the point cloud from IOP-elevated volume. (**C**) Polynomial curves that are fitted to the point clouds in the nasal–temporal direction (*green*) and superior–inferior direction (*blue*).

choroidal vessel landmarks to accurately align the two volumes.

In brief, we employed our deep learning algorithm to isolate the choroid tissue from the surrounding volume. The algorithm, trained on macula images, accurately segmented each B-scan into distinct tissue groups: the prelamina tissue (encompassing the retina), the choroid, and the sclera (Figs. 1B, 1C). Subsequently, we generated a maximum

Investigative Ophthalmology & Visual Science

projected image specifically highlighting the choroidal tissue (Figs. 1D, 1E).

Subsequently, we tasked two expert observers, TC and FAB, with marking three pairs of choroidal vessel bifurcations in both the baseline and IOP-elevated scans (Figs. 1D, 1E). It should be noted that the identified bifurcations might vary between observers, as they had the freedom to mark any conspicuous bifurcations in the pair of images. The recorded locations of the vessel bifurcations were denoted as (x, y) coordinates.

Three pairs of coordinates that were marked (Figs. 1D, 1E) were then used to determine the rotation and translation required to align the IOP-elevated volume with the baseline volume. Further details about this procedure, including the equations used and interobserver reliability, are provided in Supplementary Appendix A.

Extracting the Choroid–Sclera Interface

For each pair of baseline volume and aligned IOP-elevated volume, we extracted the choroid–sclera interface, defined as the pixels along the posterior border of the choroid tissues (Fig. 2A).

We proceeded to sample points along the choroid–sclera border at every fifth A-scan, yielding approximately 7000 points that represented the choroid–sclera interface for each OCT volume. The resulting point cloud illustrating the choroid–sclera interface is depicted in Figure 2B.

Quantifying the Changes in Macula Curvature

To quantify changes in macula curvature, we divided the curvature comparisons into two directions: the nasal–temporal direction and the superior–inferior direction. We applied a second-degree polynomial function to fit the point clouds along these directions (Fig. 2C).

We fitted 26 polynomial curves in the nasal–temporal direction and 20 polynomial curves in the superior–inferior direction. These curves were evenly distributed across the nasal–temporal and superior–inferior axes (Fig. 2C). We employed multiple second-order polynomials (rather than a single polynomial with two variables for the entire surface) to enable a more localized analysis. This approach also allowed us to vary the number of polynomials along the nasal–temporal and inferior–superior directions, effectively matching the resolution of the OCT volumes.

To calculate the curvature of each polynomial line, we employed the following equation:

$$K = \frac{|y''(m)|}{\left(1 + \left(y'(m)\right)^2\right)^{\frac{3}{2}}}$$

where K is the curvature value, m is the minimum location of the polynomial, $y'(m)$ is the first derivative of the polynomial function evaluated at m, and $y''(m)$ is the second derivative of the polynomial function evaluated at m. This equation is a well-known definition of curvature for a second-degree polynomial function.

To quantify curvature changes in an individual subject, we initially calculated the absolute curvature (K) difference between the corresponding polynomial curves in the baseline and IOP-elevated volumes. Subsequently, we determined the mean of the curvature changes in both the nasal–temporal and superior–inferior directions.

Consistent with our prior deformation tracking studies,[18,23] we assessed the baseline error of our methods by quantifying curvature changes in repeated baseline scans (five pairs). Our findings revealed minimal baseline error in curvature changes (0.3×10^{-5} µm in the nasal–temporal direction and 0.8×10^{-5} µm in the superior–inferior direction) compared to the observed curvature changes with IOP elevation. The observed baseline error amounted to approximately 4% of the mean value of curvature alterations in the nasal–temporal direction and 5% of the mean value of curvature alterations along the superior–inferior direction.

Variations in camera positioning in relation to the eye between follow-up scans could result in some image distortions, potentially introducing a bias to our reported curvature values.[25] To assess this, we utilized a simple optical model based on the work of Kuo et al.[26] to simulate the real OCT scan paths and recover the true shape of ocular structures in posterior segment OCT. We simulated relevant clinical scenarios, such as moving 3 mm closer or farther away from the machine or a lateral shift of 3 mm. From these calculations, we observed a maximum distortion of 50 μm between two follow-up scans, leading to a negligible change in global curvature. Additionally, we performed repeatability tests on baseline OCT scans, revealing minimal error in curvature values (~5% of the mean values) between two follow-up scans. Thus, the utilization of global curvature values suggests that any potential impact from OCT distortions on the results may be minimal.

Statistical Analysis

Statistical analyses were performed using R. Curvature change values (unsigned) were treated as continuous variables, and the subjects' diagnoses (control, HM, HMG, PM, and PM+S) were treated as categorical variables. We used generalized estimating equations to model our samples, accounting for between-eye correlation, age, baseline curvature, baseline IOP, and elevated IOP. Post hoc pairwise comparisons were performed to assess changes in curvature values across diagnostic groups, with significant differences reported at $P < 0.05$. Analysis of variance was used to determine differences across groups in age, axial length, visual field mean deviation (MD), pattern standard deviation (PSD), IOP on the day of the experiment, and elevated IOP.

Results

Demographics

There were significant differences ($P < 0.05$) in terms of age, axial length, and visual field (MD and PSD values) across groups (Table). Eyes in the HM group exhibited a lower average age in comparison to other groups, with the HM eyes averaging 57 years, while the eyes in the remaining groups had an average age of 61 years. As expected, myopic eyes (HM, HMG, PM, and PM+S) exhibited a higher axial length as compared to the control group. HMG, PM, and PM+S had poorer visual field indices (a more negative MD and a more positive PSD) as compared to the HM and control groups. There were no significant differences in presenting IOP on the day of the experiment and elevation across groups.

Investigative Ophthalmology & Visual Science

Table. Characteristics of Eyes in Each Group

Characteristic	Mean ± SD or *n* (%)				
	Control	HM	HMG	PM	PM+S
Age, y	64 ± 5	57 ± 6	60 ± 8	61 ± 8	63 ± 7
Sex, female, %	58	53	50	36	44
Axial length, mm	23.8 ± 1.0	26.8 ± 1.0	27.8 ± 2.5	29.7 ± 2.5	31 ± 2.3
Visual field, MD, dB	−1.2 ± 2.5	−1.27 ± 3.0	−7.4 ± 5.5	−6.1 ± 2.8	−10.4 ± 7.1
Pattern standard deviation, dB	2.2 ± 1.5	2.18 ± 1.2	6.2 ± 3.8	5.2 ± 2.7	6.6 ± 2.82
IOP on the day of the experiment,* mm Hg	15.6 ± 2.0	15.6 ± 2.3	16.3 ± 2.8	16.0 ± 2.8	17.2 ± 3.3
Elevated IOP, mm Hg	38.5 ± 7	37.6 ± 7	38.6 ± 6	37.6 ± 7	37.8 ± 7

* IOP after treatment (for HMG eyes).

Changes in Macula Curvature Along the Nasal–Temporal Direction

Along the nasal–temporal direction, we observed significantly higher macula curvature changes in the PM+S (13.5 ± 8.2 × 10^{-5} μm^{-1}), PM (9.0 ± 7.9 × 10^{-5} μm^{-1}), and HMG (5.2 ± 5.1 m × 10^{-5} μm^{-1}) eyes as compared to HM (3.1 ± 2.7 × 10^{-5} μm^{-1}) eyes (Fig. 3) under IOP elevation. We observed no significant difference in macula curvature changes between control eyes (4.2 ± 4.3 × 10^{-5} μm^{-1}) and HM eyes. We also found no significant differences in macula curvature changes between HMG eyes and control eyes.

Changes in Macula Curvature Along the Superior–Inferior Direction

Along the superior–inferior direction, we found no significant differences in macula curvature changes across all groups. On average, we observed significantly higher macula curvature changes in the superior–inferior direction (12.8 ± 9.2 × 10^{-5} μm^{-1}) than in the nasal–temporal direction (6.2 ± 5.7 × 10^{-5} μm^{-1}).

Macula Exhibited Both Flattening and Concaving Behavior Under IOP Elevation

We observed that, in response to elevated IOP, the macula demonstrated a variable change in curvature, becoming more concave or flatter. On average, across all eyes, the macula exhibited increased curvature (concavity) in both nasal–temporal and superior–inferior directions, with a mean curvature increase (both directions) measuring 0.8 ± 15.0 × 10^{-5} μm^{-1}. Eyes with PM+S, PM, and HMG exhibited an increase in curvature (concavity) in both directions, while eyes with HM and controls exhibited a decrease in curvature (flattening) in both directions in response to IOP elevation.

Discussion

In this study, we quantified the IOP-induced deformation of the choroid–sclera interface at the macula region in terms of curvature changes. We found that (1) PM eyes and HMG eyes had significantly more curvature changes along the nasal–temporal direction than HM eyes, and (2) we did not observe significant differences in curvature changes along superior–inferior direction. Our findings suggest that the macula of PM eyes and HMG eyes were particularly sensitive to IOP elevation and that the curvature changes of the sclera–choroid interface along the nasal–temporal direction may be useful in assessing the robustness of the macula region in highly myopic eyes.

We observed that the nasal–temporal macula curvature changes in eyes with HMG were significantly higher than in eyes with HM alone. This finding is consistent with our earlier study, which reported that the ONH of eyes with HMG deformed more under acute IOP elevation than eyes with HM.[8] This phenomenon may be attributed to the interaction of two distinct biomechanical pathways. On one hand, there is a weakening of the macula region due to myopia-related remodeling (scleral thinning,[27,28] tissue loss,[28] and an increase in small-diameter collagen fibrils[28]). On the other hand, glaucoma induces complex tissue remodeling, including excavation of the LC, an increase in connective tissue volume, and scleral stiffening, ultimately leading to ocular rigidity.[29] The biomechanical interactions between these two pathways remain unclear, but we did not observe a stiffening response, as the net effect of these interactions was an elevated structural vulnerability of the macula to a sudden increase in IOP. It is noteworthy that while glaucoma generally induces a stiffening response in the ONH, early glaucoma could result in hypercompliance in the LC and peripapillary sclera.[30,31] Given that most of our patients with HMG were in the early to moderate glaucoma stage, the ONH may still be in the compliance phase. Furthermore, Jonas et al.[32] found that in HM eyes, the presence of glaucoma was associated with a thinner LC compared to non-HM eyes. As the LC serves as a crucial loadbearing structure of the ONH, this may contribute indirectly to the observed weakening of the macula in our study.[33,34] Despite these findings, limited evidence exists regarding structural changes in the macula during glaucoma progression, primarily due to challenges in isolating confounding factors such as age and myopia-related macular changes.[35] Most studies on structural changes in the macula have focused on parameters such as ganglion cell/layer thickness or macula thickness, neglecting the relatively understudied role of the sclera, the primary supporting tissue.[36,37] The biomechanics of the macula, influenced by both glaucoma and high myopia, may involve a multifaceted interplay of factors beyond scleral stiffening. Further research on the interaction between glaucoma and myopia is warranted to gain a deeper understanding of this aspect.

We observed that the nasal–temporal macula curvature changes in PM and PM+S eyes were higher than in HM eyes and controls. PM, especially when accompanied by staphyloma(s), is commonly associated with myopic traction maculopathy and myopic macular degeneration.[38,39] The presence of myopic traction maculopathy and/or staphyloma in PM eyes is closely linked to thinning and elongation of the

Investigative Ophthalmology & Visual Science

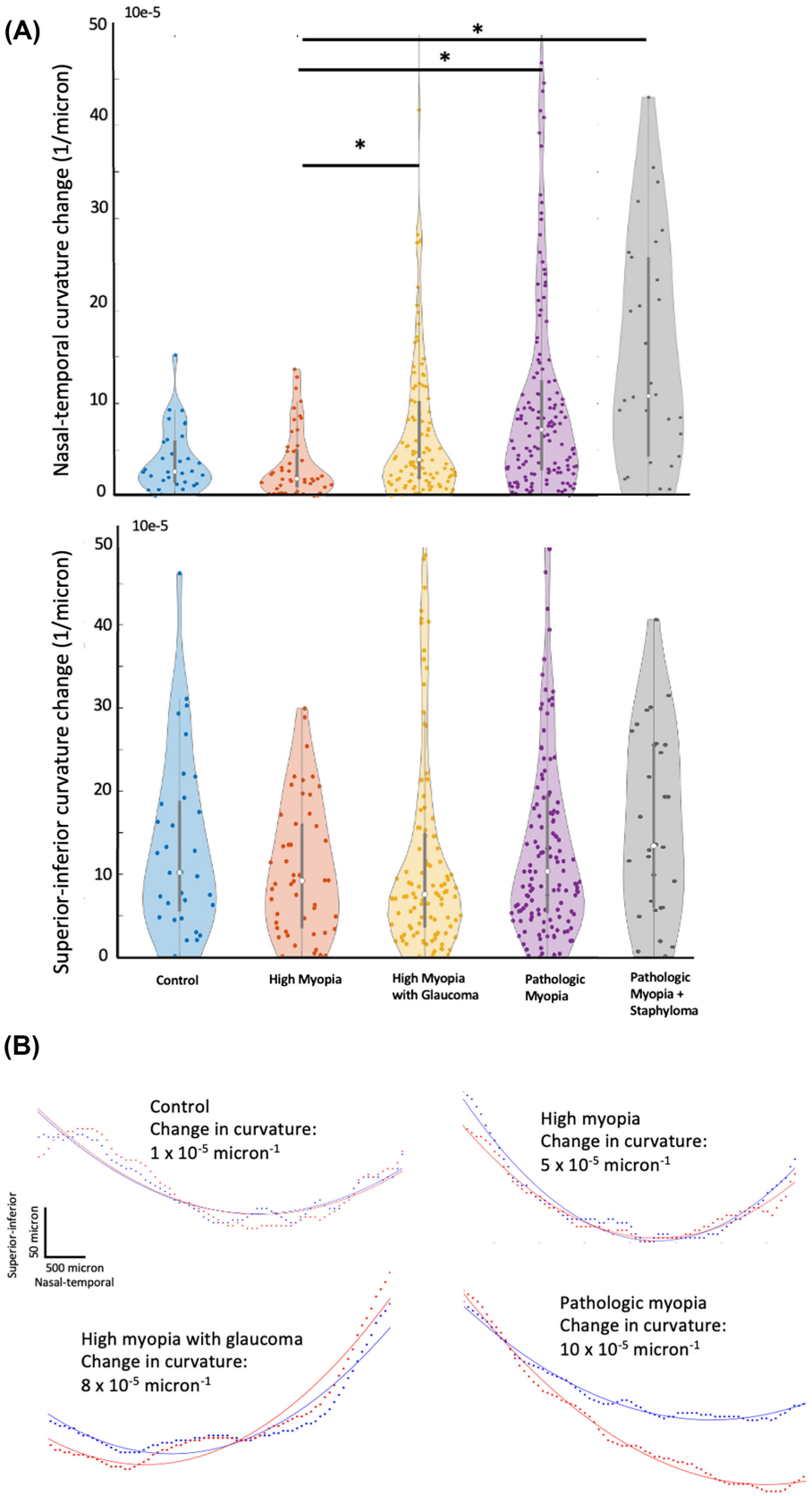

Figure 3. (**A**) A violin plot presenting a comparison of mean macula curvature change in the (a) nasal–temporal direction and (b) superior–inferior direction (* denotes significant differences between two groups, $P < 0.05$). (**B**) Illustration of curvature changes for each diagnostic group. The central slices of the macula are depicted along the nasal–temporal direction. *Blue lines* represent baseline scans, while *red lines* represent IOP-elevated scans. *Dotted lines* indicate the segmented choroid–scleral interface, and *solid lines* represent the fitted polynomial curve.

Investigative Ophthalmology & Visual Science

local sclera, along with structural deformities in the posterior ocular segment.[40] The adverse remodeling of the sclera and the structural deformities may precipitate further structural weakening of the ocular globe,[41] potentially forming a positive feedback loop that diminishes scleral resistance to subsequent outpouching. Norman et al.[9] demonstrated that a thinner posterior sclera is more prone to deformation, leading to larger expansions of the scleral canal and deformation of the LC compared to cases with a thicker sclera. Moreover, within our patients with PM, posterior pole staphyloma and peripapillary staphyloma emerge as the predominant staphyloma types. The existence of these staphylomas could disrupt the circumferential alignment of collagen fibers at the peripapillary sclera, as highlighted previously by other groups.[42] This disruption carries the inherent risk of intensifying scleral weakening, ultimately contributing to posterior macula deformation characterized by an increase in macular curvature under elevated IOP, as observed in our study.

Remarkably, we observed a significant difference in macula curvature change in the nasal–temporal direction but not in the superior–inferior direction. Existing literature establishes that the collagen fiber arrangement around the peripapillary region is predominantly circumferential,[43–45] forming a reinforcing ring that restrains ONH deformation under elevated IOP. A meridional arrangement of collagen fibers has been identified away from the ONH region,[46,47] speculated to resist extraocular muscle forces or limit axial elongation of the globe in myopia. Our results showed a distinct weakening of the macula in a meridional direction (nasal–temporal), aligning with the direction of myopia progression. Interestingly, studies also have reported misalignment (offset) of Bruch's membrane opening (BMO) plane with the anterior scleral canal opening plane, particularly in the inferior temporal or temporal direction in myopic eyes. The directional-dependent remodeling of the ONH structure during myopia development also suggests a weakening of the ONH in the nasal direction. Thus, we postulate that there are direction-specific structural disturbances affecting the loadbearing components of macular tissues during the advancement of conditions such as HM and/or the onset of glaucoma.[42,48]

While we did not observe significant macula curvature changes in the superior–inferior direction, it should be noted that the curvature changes in this axis were, in fact, significantly higher than those in the nasal–temporal direction. This implies that the macula is more susceptible to acute IOP elevation along the superior–inferior direction, a characteristic seemingly consistent across our subject groups. To our knowledge, there is no existing literature that compares IOP-induced deformation between these two axes in the macula. However, drawing parallels from our earlier study on the ONH, we reported that curvature changes were generally more pronounced in the superior–inferior direction than in the nasal–temporal direction.[24]

When analyzing the direction of macular curvature changes (signed), we observed that the macula could become either more concave or flatter across all subject groups. On average, the magnitude of this change was small (0.8×10^{-5} μm^{-1}), indicating a slight tendency for the macula to become more concave under elevated IOP. This occurs because curvature changes can vary in direction within a single individual, with some regions becoming more concave and others flattening. As a result, averaging these directional changes tends to neutralize the overall value and obscure the differences in deformation between groups. This finding is consistent with our previous work on the ONH, where average signed strain values (compressive or tensile) were also small across subject groups.[23] Additionally, other studies have shown that the ONH can displace both anteriorly and posteriorly under elevated IOP.[49,50] Therefore, we believe that unsigned curvature change is a more effective measure for distinguishing differences between our groups of interest, as it more accurately reflects the magnitude of mechanical forces experienced by the tissues.

This study has several limitations worth considering. First, we utilized a simplified approach to quantify deformation changes, deviating from our previous studies that employed the three-dimensional digital volume correlation (DVC) algorithm.[18,23] The rationale behind this decision stems from the absence of distinct features in the macula, such as central retinal vessel trunks, BMO, and the LC, which are necessary for optimal performance of DVC. Instead, we opted for a geometric approach, similar to previous studies that utilized LC–global shape index,[51,52] LC depth,[53] and peripapillary sclera angle to characterize the ONH structure. We believe that this approach provided a suitable initial approximation of the macular deformation. In the future, we intend to incorporate a comprehensive three-dimensional deformation tracking methodology as DVC validation advances, particularly in ex vivo samples of the macula.

Third, we employed a manual landmark (vessel bifurcations) identification to assist in the alignment of the OCT volumes, instead of using an automatic registration algorithm used in our previous works.[18,23] This again was due to the lack of high-contrast landmarks in the macula region that adversely affect the performance of the registration algorithm. We used macular vessel bifurcations as alignment landmarks, unlike retinal vessels commonly used in other studies, because our scan area, centered on the fovea, lacks retinal vessels. Notably, vessel-based registration was used in several other studies to align fundus images and OCT volumes with good performance,[54,55] and we believe that the low variability between observers (Supplementary Appendix A) showed that it was sufficient for our application.

Fourth, we utilized a second-degree polynomial fit to approximate the macula curvatures, which may not offer an optimal fit. However, our findings demonstrate that the error associated with the second-degree polynomial is deemed acceptable. It is important to note that, thus far, no standardized methods for assessing macula shape have been established. Some studies have employed cubic spline interpolation,[56,57] yielding comparable curvature values (around 8×10^{-5} μm^{-1}) to our results. Given the current constraints in knowledge, we believe that a simple approximation is preferable, and a lower-order polynomial is also less sensitive to data noise.

Fifth, the utilization of ophthalmodynamometry in our study could introduce experimental errors as it involved applying external force to the anterior sclera through the eyelid. We have extensively discussed this issue in our previous work.[23] In summary, the elevated IOP can vary due to factors such as the outflow facility[58] and the individual biomechanical characteristics of each eye, including variations in axial length.[59] Moreover, IOP fluctuates during the duration of the scan due to the presence of an ocular pulse.[60] Additionally, the actual level of IOP attained through ophthalmodynamometry may potentially decrease during the time required for OCT acquisition.[61] This decline could

Investigative Ophthalmology & Visual Science

also vary among subjects, depending on the outflow facility[58] and the biomechanical characteristics[59] of each eye. The use of an ophthalmodynamometer can also affect the shape of the lens and cornea and, consequently, its optics. This may introduce bias in our curvature values due to differences in OCT image distortion with and without ophthalmodynamometer (ODM). However, our measurements showed that the changes in corneal curvature, lens curvature, and corneal thickness were minimal. Therefore, we believe these factors should not significantly impact the reported trends.

Lastly, our patients with HM were younger compared to other groups. This could have resulted in a different biomechanical status of HM groups (e.g., more compliant sclera).[62] However, we believe this would not significantly affect our result since our subjects were from an older population (more than 50 years of age). Age-related changes in scleral elastin fibers and extracellular matrix should have occurred at an earlier age.[63] Additionally, we accounted for age in our statistical model, so the reported differences have already considered age. Nonetheless, age remains a significant factor in studies dealing with biomechanics, and to our knowledge, no current studies have quantified macular deformation with respect to age. This could be a valuable topic for further investigation.

In conclusion, our study indicates that changes in macula curvature under IOP elevation may reflect the biomechanical integrity of the macula in a clinical context. While these findings are preliminary and suggest correlation rather than causation, they highlight the potential biomechanical interplay between glaucoma and myopia in the macular region.

Acknowledgments

Supported by National Medical Research Council (MOH-000531-00 [QVH] and MOH-001103-00 [QVH]); the SERI-Lee Foundation (LF0621-1 [QVH]); the Lee Foundation (TLF1021-3 [QVH] and TLF 0322-8 [QVH]); the SingHealth Foundation-SNEC (R1499/82/2017 [QVH]) in Singapore; the Singapore Ministry of Education, Academic Research Funds, Tier 2 (R-397-000-280-112; R-397-000-308-112); Singapore Ministry of Education, Academic Research Funds, Tier 1 (R-397000-294-114); the National Medical Research Council (Grant NMRC/STAR/0023/2014); National Natural Science Foundation of China (12002025); Tracking and Reducing Glaucoma Blindness with Emerging Technologies (TARGET, MOH-OFLCG21jun-0003); and the Retinal Analytics through Machine learning aiding Physics (RAMP) project supported by the National Research Foundation, Prime Minister's Office, Singapore, under its Intra-Create Thematic Grant "Intersection of Engineering and Health" (NRF2019-THE002-0006), awarded to the Singapore MIT Alliance for Research and Technology (SMART) Centre.

Disclosure: **T. Chuangsuwanich**, None; **T.A. Tun**, None; **F.A. Braeu**, None; **R.S. Chong**, None; **X. Wang**, None; **C.-L. Ho**, None; **T. Aung**, None; **M.J.A. Girard**, Abyss Processing Pte Ltd (O); **Q.V. Hoang**, None

References

1. McBrien NA, Jobling AI, Gentle A. Biomechanics of the sclera in myopia: extracellular and cellular factors. *Optom Vis Sci*. 2009;86(1):E23–E30.
2. Flores-Moreno I, Puertas M, Ruiz-Medrano J, et al. Influence of posterior staphyloma in myopic maculopathy and visual prognosis. *Eye*. 2024;38(1):145–152.
3. Ikuno Y. Overview of the complications of high myopia. *Retina*. 2017;37(12):2347–2351.
4. Spaide RF, Wong D, Fisher Y, Goldbaum M. Correlation of vitreous attachment and foveal deformation in early macular hole states. *Am J Ophthalmol*. 2002;133(2):226–229.
5. Park SH, Park KH, Kim HY, et al. Square grid deformation analysis of the macula and postoperative metamorphopsia after macular hole surgery. *Retina (Philadelphia, Pa)*. 2021;41(5):931.
6. Kumagai K, Hangai M, Larson E, Ogino N. Vitreoretinal interface and foveal deformation in asymptomatic fellow eyes of patients with unilateral macular holes. *Ophthalmology*. 2011;118(8):1638–1644.
7. Chuangsuwanich T, Hung PT, Wang X, et al. Morphometric, hemodynamic, and biomechanical factors influencing blood flow and oxygen concentration in the human lamina cribrosa. *Invest Ophthalmol Vis Sci*. 2020;61(4):3.
8. Chuangsuwanich T, Tun T, Braeu F, et al. How myopia and glaucoma influence the biomechanical susceptibility of the optic nerve head. bioRxiv 2022:2022.12. 19.520997, https://iovs.arvojournals.org/article.aspx?articleid=2791379.
9. Norman RE, Flanagan JG, Sigal IA, et al. Finite element modeling of the human sclera: influence on optic nerve head biomechanics and connections with glaucoma. *Exp Eye Res*. 2011;93(1):4–12.
10. McBrien NA, Gentle A. Role of the sclera in the development and pathological complications of myopia. *Prog Retin Eye Res*. 2003;22(3):307–338.
11. Levy AM, Fazio MA, Grytz R. Experimental myopia increases and scleral crosslinking using genipin inhibits cyclic softening in the tree shrew sclera. *Ophthalmic Physiol Opt*. 2018;38(3):246–256.
12. Grytz R, Yang H, Hua Y, et al. Connective tissue remodeling in myopia and its potential role in increasing risk of glaucoma. *Curr Opin Biomed Eng*. 2020;15:40–50.
13. Shen L, Melles RB, Metlapally R, et al. The association of refractive error with glaucoma in a multiethnic population. *Ophthalmology*. 2016;123(1):92–101.
14. Perera SA, Wong TY, Tay W-T, et al. Refractive error, axial dimensions, and primary open-angle glaucoma: the Singapore Malay Eye Study. *Arch Ophthalmol*. 2010;128(7):900–905.
15. Grødum K, Heijl A, Bengtsson B. Refractive error and glaucoma. *Acta Ophthalmol Scand*. 2001;79(6):560–566.
16. Chang RT, Singh K. Myopia and glaucoma: diagnostic and therapeutic challenges. *Curr Opin Ophthalmol*. 2013;24(2):96–101.
17. Shin H-Y, Park H-YL, Park CK. The effect of myopic optic disc tilt on measurement of spectral-domain optical coherence tomography parameters. *Br J Ophthalmol*. 2015;99(1):69–74.
18. Chuangsuwanich T, Tun TA, Braeu FA, et al. Adduction induces large optic nerve head deformations in subjects with normal-tension glaucoma. *Br J Ophthalmol*. 2024;108(4):522–529.
19. Ohno-Matsui K, Kawasaki R, Jonas JB, et al. International photographic classification and grading system for myopic maculopathy. *Am J Ophthalmol*. 2015;159(5):877–883.e7.
20. Nagaoka N, Jonas JB, Morohoshi K, et al. Glaucomatous-type optic discs in high myopia. *PLoS One*. 2015;10(10):e0138825.
21. Wang X, Beotra MR, Tun TA, et al. In vivo 3-dimensional strain mapping confirms large optic nerve head deformations following horizontal eye movements. *Invest Ophthalmol Vis Sci*. 2016;57(13):5825–5833.
22. Beotra MR, Wang X, Tun TA, et al. In vivo three-dimensional lamina cribrosa strains in healthy, ocular hypertensive, and glaucoma eyes following acute intraocular pressure elevation. *Invest Ophthalmol Vis Sci*. 2018;59(1):260–272.

23. Chuangsuwanich T, Tun TA, Braeu FA, et al. Differing associations between optic nerve head strains and visual field loss in normal- and high-tension glaucoma subjects. *Ophthalmology*. 2023;130(1):99–110.
24. Tun TA, Thakku SG, Png O, et al. Shape changes of the anterior lamina cribrosa in normal, ocular hypertensive, and glaucomatous eyes following acute intraocular pressure elevation. *Invest Ophthalmol Vis Sci*. 2016;57(11):4869–4877.
25. Grytz R, El Hamdaoui M, Fuchs PA, et al. Nonlinear distortion correction for posterior eye segment optical coherence tomography with application to tree shrews. *Biomed Opt Express*. 2022;13(2):1070–1086.
26. Kuo AN, McNabb RP, Chiu SJ, et al. Correction of ocular shape in retinal optical coherence tomography and effect on current clinical measures. *Am J Ophthalmol*. 2013;156(2):304–311.
27. Phillips J, McBrien N. Form deprivation myopia: elastic properties of sclera. *Ophthalmic Physiol Opt*. 1995;15(5):357–362.
28. McBrien NA, Cornell LM, Gentle A. Structural and ultrastructural changes to the sclera in a mammalian model of high myopia. *Invest Ophthalmol Vis Sci*. 2001;42(10):2179–2187.
29. Liu B, McNally S, Kilpatrick JI, et al. Aging and ocular tissue stiffness in glaucoma. *Surv Ophthalmol*. 2018;63(1):56–74.
30. Ivers KM, Yang H, Gardiner SK, et al. In vivo detection of laminar and peripapillary scleral hypercompliance in early monkey experimental glaucoma. *Invest Ophthalmol Vis Sci*. 2016;57(9):OCT388–OCT403.
31. Burgoyne CF, Downs JC, Bellezza AJ, et al. The optic nerve head as a biomechanical structure: a new paradigm for understanding the role of IOP-related stress and strain in the pathophysiology of glaucomatous optic nerve head damage. *Prog Retin Eye Res*. 2005;24(1):39–73.
32. Jonas JB, Berenshtein E, Holbach L. Lamina cribrosa thickness and spatial relationships between intraocular space and cerebrospinal fluid space in highly myopic eyes. *Invest Ophthalmol Vis Sci*. 2004;45(8):2660–2665.
33. Sigal I, Yang H, Roberts M, et al. The effect of lamina cribrosa thickness and position on optic nerve head biomechanics. *Invest Ophthalmol Vis Sci*. 2008;49(13):3668.
34. Midgett D, Liu B, Ling YTT, et al. The effects of glaucoma on the pressure-induced strain response of the human lamina cribrosa. *Invest Ophthalmol Vis Sci*. 2020;61(4):41.
35. Nouri-Mahdavi K, Weiss RE. Detection of glaucoma deterioration in the macular region with optical coherence tomography: challenges and solutions. *Am J Ophthalmol*. 2021;222:277–284.
36. Mohammadzadeh V, Rabiolo A, Fu Q, et al. Longitudinal macular structure–function relationships in glaucoma. *Ophthalmology*. 2020;127(7):888–900.
37. Schlottmann PG, De Cilla S, Greenfield DS, et al. Relationship between visual field sensitivity and retinal nerve fiber layer thickness as measured by scanning laser polarimetry. *Invest Ophthalmol Vis Sci*. 2004;45(6):1823–1829.
38. Frisina R, Gius I, Palmieri M, et al. Myopic traction maculopathy: diagnostic and management strategies. *Clin Ophthalmol*. 2020;14:3699–3708.
39. Ohno-Matsui K. Pathologic myopia. *Asia Pac J Ophthalmol*. 2016;5(6):415–423.
40. Maruko I, Iida T, Sugano Y, et al. Morphologic analysis in pathologic myopia using high-penetration optical coherence tomography. *Invest Ophthalmol Vis Sci*. 2012;53(7):3834–3838.
41. Jonas JB, Ohno-Matsui K, Holbach L, Panda-Jonas S. Histology of myopic scleral staphylomas. *Invest Ophthalmol Vis Sci*. 2019;60(9):4354.
42. Markov PP, Eliasy A, Pijanka JK, et al. Bulk changes in posterior scleral collagen microstructure in human high myopia. *Mol Vis*. 2018;24:818.
43. Strouthidis NG, Girard MJ. Altering the way the optic nerve head responds to intraocular pressure—a potential approach to glaucoma therapy. *Curr Opin Pharmacol*. 2013;13(1):83–89.
44. Girard MJ, Suh J-KF, Bottlang M, et al. Scleral biomechanics in the aging monkey eye. *Invest Ophthalmol Vis Sci*. 2009;50(11):5226–5237.
45. Jan N-J, Lathrop K, Sigal IA. Collagen architecture of the posterior pole: high-resolution wide field of view visualization and analysis using polarized light microscopy. *Invest Ophthalmol Vis Sci*. 2017;58(2):735–744.
46. Willemse J, Gräfe MG, Verbraak FD, de Boer JF. In vivo 3D determination of peripapillary scleral and retinal layer architecture using polarization-sensitive optical coherence tomography. *Transl Vis Sci Technol*. 2020;9(11):21.
47. Gogola A, Jan N-J, Lathrop KL, Sigal IA. Radial and circumferential collagen fibers are a feature of the peripapillary sclera of human, monkey, pig, cow, goat, and sheep. *Invest Ophthalmol Vis Sci*. 2018;59(12):4763–4774.
48. Pijanka JK, Coudrillier B, Ziegler K, et al. Quantitative mapping of collagen fiber orientation in non-glaucoma and glaucoma posterior human sclerae. *Invest Ophthalmol Vis Sci*. 2012;53(9):5258–5270.
49. Tun TA, Atalay E, Baskaran M, et al. Association of functional loss with the biomechanical response of the optic nerve head to acute transient intraocular pressure elevations. *JAMA Ophthalmol*. 2018;136(2):184–192.
50. Coleman AL, Quigley HA, Vitale S, Dunkelberger G. Displacement of the optic nerve head by acute changes in intraocular pressure in monkey eyes. *Ophthalmology*. 1991;98(1):35–40.
51. Thakku SG, Tham Y-C, Baskaran M, et al. A global shape index to characterize anterior lamina cribrosa morphology and its determinants in healthy Indian eyes. *Invest Ophthalmol Vis Sci*. 2015;56(6):3604–3614.
52. Tun TA, Wang X, Baskaran M, et al. Variation of peripapillary scleral shape with age. *Invest Ophthalmol Vis Sci*. 2019;60(10):3275–3282.
53. Park SC, Brumm J, Furlanetto RL, et al. Lamina cribrosa depth in different stages of glaucoma. *Invest Ophthalmol Vis Sci*. 2015;56(3):2059–2064.
54. Golabbakhsh M, Rabbani H. Vessel-based registration of fundus and optical coherence tomography projection images of retina using a quadratic registration model. *IET Image Process*. 2013;7(8):768–776.
55. Wu J, Gerendas BS, Waldstein SM, et al. Stable registration of pathological 3D-OCT scans using retinal vessels. Presented at the *Ophthalmic Medical Image Analysis International Workshop: University of Iowa, September 14*, 2014;1.
56. Minami S, Ito Y, Ueno S, et al. Analysis of macular curvature in normal eyes using swept-source optical coherence tomography. *Jpn J Ophthalmol*. 2020;64:180–186.
57. Komori S, Ueno S, Ito Y, et al. Steeper macular curvature in eyes with non-highly myopic retinitis pigmentosa. *Invest Ophthalmol Vis Sci*. 2019;60(8):3135–3141.
58. Kazemi A, McLaren JW, Lin S-C, et al. Comparison of aqueous outflow facility measurement by pneumatonography and digital Schiøtz tonography. *Invest Ophthalmol Vis Sci*. 2017;58(1):204–210.
59. Grytz R, Fazio MA, Girard MJ, et al. Material properties of the posterior human sclera. *J Mech Behav Biomed Mater*. 2014;29:602–617.

Investigative Ophthalmology & Visual Science

60. Dastiridou AI, Ginis HS, De Brouwere D, et al. Ocular rigidity, ocular pulse amplitude, and pulsatile ocular blood flow: the effect of intraocular pressure. *Invest Ophthalmol Vis Sci*. 2009;50(12):5718–5722.
61. Kronfeld, PC. Tonography. *AMA Arch Ophthalmol*. 1952; 48(4):393–404.
62. Geraghty B, Jones SW, Rama P, et al. Age-related variations in the biomechanical properties of human sclera. *J Mech Behav Biomed Mater*. 2012;16:181–191.
63. Boote C, Sigal IA, Grytz R, et al. Scleral structure and biomechanics. *Prog Retin Eye Res*. 2020;74:100773.

Investigative Ophthalmology & Visual Science